Cation and lone pair order-disorder in the polymorphic mixed metal bismuth scheelite $Bi_3FeMo_2O_{12}$

Matilde Saura-Múzquiz,[a, b] Frederick P. Marlton,[a] Bryce G. Mullens,[a] Jiatu Liu,[a] Thomas Vogt,[c] Helen Elizabeth Maynard-Casely,[d] Maxim Avdeev,[a,d] Douglas A. Blom[e] and Brendan J. Kennedy[a*]

[a] School of Chemistry, University of Sydney, F11, Sydney, NSW 2006, Australia
[b] Departamento de física de Materiales, Facultad de CC. Físicas, Universidad Complutense de Madrid. Plaza de Ciencias 1, Ciudad Universitaria, 28040, Madrid, Spain.
[c] Department of Chemistry & Biochemistry and NanoCenter, University of South Carolina, Columbia, South Carolina, 29208, United States
[d] Australian Centre for Neutron Scattering, ANSTO, New Illawarra Road, Lucas Heights NSW 2234 Australia
e Department of Chemical Engineering and NanoCenter, University of South Carolina, Columbia, South Carolina, 29208, United States

* To whom correspondence should be addressed: Brendan Kennedy (Brendan.Kennedy@Sydney.edu.au)

Abstract

The $Bi_3FeMo_2O_{12}$ system is examined as a rare example of a transition metal oxide which, upon heating, undergoes a symmetry lowering and 2:1 ordering of the transition metal cations. The compound was synthesised in the tetragonal scheelite structure (S.G. #88: $I4_1/a$) by a sol-gel method and converted into the monoclinic polymorph (S.G. #15: $C2/c$) by calcination above 500 °C. The structure of both polymorphs was analysed using a combination of X-ray and neutron diffraction data, and the temperature-dependent phase transition between these was investigated *in situ* using variable temperature neutron powder diffraction and scanning transmission electron microscopy. The results show that the structural phase transition takes place at low temperature (~ 500 °C) and is 1st order in nature, as evident from the coexistence of both structures. The transition from tetragonal to monoclinic results in reduction of the equivalent unit cell volume. The role of the Bi^{3+} 6s lone pairs in the temperature-driven phase transition has been studied using neutron pair distribution function analysis. Local structure analysis *via* neutron total scattering revealed the Bi^{3+} 6s lone pairs to be stereochemically active in both structures, with short

correlation lengths in the tetragonal structure and long correlation lengths in the monoclinic structure, leading to the facile phase conversion and to a more efficient packing density with highly correlated lone pairs in the monoclinic structure. Magnetization isotherms of the tetragonal structure collected at 1.8 K exhibit ferromagnetic behavior, suggesting that the interplay between the observed short-range monoclinic order, defects and surface-to-bulk effects alters the magnetic interaction, leading to short range ferromagnetic interactions, which is highly unexpected given the low temperature antiferromagnetic order observed in the monoclinic structure.

Introduction

Lone pair electrons can exert significant structural and electronic influence on chemical species, ranging from nominally simple systems such as H_2O to compositionally complex oxides such as PZT, $(PbZr_{1-x}Ti_x)O_3$. The heavier sixth row elements (Tl-Bi) with a $6p^06s^2$ configuration are of special interest to the broad materials chemistry community since the stereochemical activity of the lone pairs can result in an asymmetric coordination environment around the cation leading to unique properties. Density functional theory has been successfully used to rationalise the appearance of stereochemically active lone pair, although anomalies exist. For example, $TlReO_4$ and $BiVO_4$ both display crystal structures consistent with a stereochemically active lone pair, but $PbWO_4$ does not, rather in $PbWO_4$ the 6s electrons are temporally and spatially averaged resulting in spherical symmetry of the isolated s orbital, seemingly playing no structure-directing role. The formation of stereochemically active lone pairs is dependent on the strength of the interaction between the cation s- and anion p-states. [1, 2] This interaction increases as the energy difference between the states decrease, favouring structure-directing long-range ordering of lone pair electrons. Since the energy of the metal s-orbitals decreases as the effective nuclear charge increase, Tl > Pb > Bi the weakest overlap will be in Bi oxides. Whereas Tl^+ and Pb^{2+} are toxic the isoelectronic Bi^{3+} cation has very low toxicity of Bi^{3+} making this an attractive alternate to Pb^{2+} for use in functional materials.

It has been proposed that correlated disorder can result in lower local symmetry than the (higher) average symmetry imposed by the crystal lattice. Such local symmetry changes persist only in a high-temperature high average symmetry state and as seen in PZT long range ordering of the lone-pairs only emerges upon cooling.[3] Very rarely a low-symmetry state emerges from the high-symmetry state upon heating, by virtue of a well-defined displacement of atoms from their centrosymmetric positions. This

phenomenon has been called *emphanisis* and has been observed in systems containing cations with lone pair electrons. For example, emphanisis is associated with the thermoelectric properties of the binary lead chalcogenides and is believed to be responsible for the unusual re-entrant behaviour of $TlReO_4$.[4, 5] Lone-pair induced emphanisis has also been observed in $CsSnBr_3$.[6]

The bismuth molybdate $Bi_3FeMo_2O_{12}$ is a rare example of an oxide that undergoes a symmetry lowering transition (from tetragonal to monoclinic) upon heating.[7] The role of the Bi^{3+} $6s^2$ lone-pair electrons in this transition has not been established. Bismuth molybdates are used as selective oxidation catalysts for the synthesis of acrolein, which is an important precursor for the industrial production of acrylic acid and methionine, and for the ammoxidation of propene to produce acrylonitrile.[8] Three main bismuth molybdate phases, with different Bi/Mo ratios are of interest, namely α-$Bi_2Mo_3O_{12}$, β-$Bi_2Mo_2O_9$, and γ-Bi_2MoO_6.[9-11] The first two of these have defect and scheelite-like structures whilst γ-Bi_2MoO_6 has a layered Aurivillius structure. The scheelite-type phases are often considered catalytically more active.[12] The mixed Bi-Fe-Mo system, which also has a scheelite-like phase namely $Bi_3FeMo_2O_{12}$, has also been studied for use as a catalyst.[7] The scheelites are a family of compounds with chemical formula ABO_4, named for the mineral scheelite $CaWO_4$, where A is a large low valent cation and B a smaller high valent cation.[13] The archetypal scheelite crystal structure is tetragonal in space group $I4_1/a$ (#88) and consists of isolated BO_4 tetrahedra surrounded by AO_8 dodecahedra. This structure supports a large variety of atomic radii and charge combinations of the cations, making it a versatile structure that can exhibit a diverse range of physical and electronic properties. In addition to their uses as heterogenous catalysts scheelite-type oxides including $CaWO_4$, $BiVO_4$ and $NaLa(MoO_4)_2$ have been extensively studied for a range of applications exploiting properties such as luminescence,[14, 15] ferroelectricity[16] and ionic conductivity.[17, 18] Bi^{3+} containing scheelites have also been shown to be efficient photocatalysts due to the strong repulsive force of the $6s^2$ lone pair of Bi^{3+}, resulting in distortion of the BO_4 tetrahedra and alteration of the band gap.[19-22]

The tetragonal scheelite structure is most commonly observed for cation size ratios of $r_A/r_B \sim 2.75$,[23] and variations in this ratio can result in lower symmetry structures.[24-26] Given that the intrinsic physical properties of functional materials are ultimately determined by the material's atomic structure, many studies have been conducted on the structure, phase transitions and properties of stoichiometric scheelite-type structures.[27-30] Several types of non-stoichiometric scheelites also exist. The most common ones have A-site vacancies, as seen in α-$Bi_2Mo_3O_{12}$, or partial substitution of the oxygen anions by F or N.[31] Another class of non-stoichiometric scheelites are those containing two different cations on the B-site. These are much rarer and far less literature exists regarding their structure and properties. An example is $Bi_3FeMo_2O_{12}$, which was reported by Sleight *et al.* in 1974 as the first scheelite-type compound containing trivalent cations on the tetrahedral sites.[32] In 1975, Jeitschko *et al.* reported that two different polymorphs of $Bi_3FeMo_2O_{12}$ could be isolated.[7] In their study, a tetragonal scheelite-type polymorph was prepared by a

wet chemical route from aqueous solution of the constituent ions. It was reported that when this tetragonal scheelite phase was heated above 600 °C, a 2:1 ordering of the Mo and Fe cations occurred, which lowered the symmetry to monoclinic in space group $C2/c$ (#15). This structure is of particular interest because, while ordering of the A cations has been described in $A^+A'^{3+}[Mo(W)O_4]_2$ scheelites,[33, 34] $Bi_3FeMo_2O_{12}$, together with the recently described double scheelite La_2SiMoO_8[35], is a rare example where the ordering occurs in the tetrahedral sites. The structures of the polymorphs of $Bi_3FeMo_2O_{12}$ are represented in Figure 1.
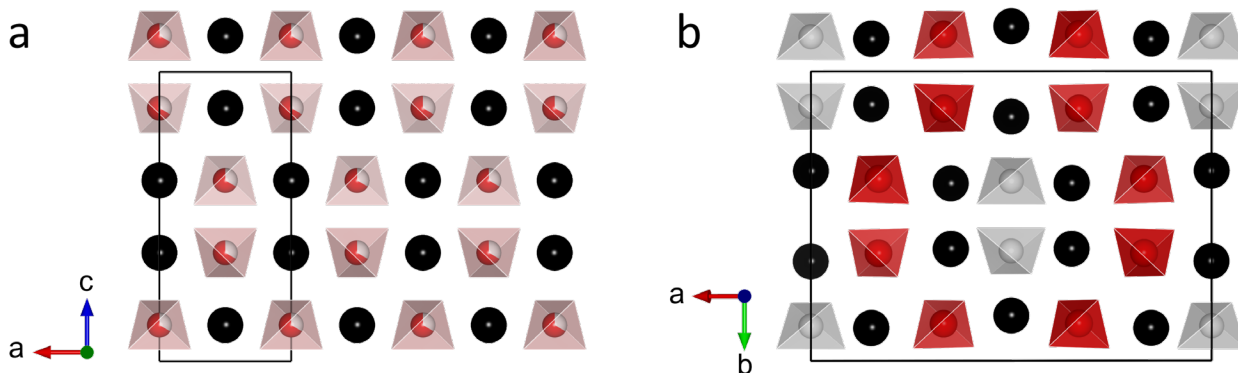

Figure 1: Representation of the crystal structure of a) low-temperature disordered tetragonal ($I4_1/a$, archetypal scheelite) and b) high-temperature ordered monoclinic ($C2/c$) polymorphs of $Bi_3FeMo_2O_{12}$. The tetrahedra represent the coordination environment of the Fe (grey) and Mo (red) cations. The Bi cations are represented in black. The oxygen atoms (not shown) are located at the corners of the tetrahedra.

The scheelite $TlReO_4$ also presents with a 2:1 ordering, but in this case it is through differing rotations of the $[ReO_4]$ tetrahedra.[24] The observed 2:1 rotation pattern of the ReO_4 tetrahedra, can be viewed as analogous to the 2:1 chemical ordering of the $[MoO_4]$ and $[FeO_4]$ tetrahedra in monoclinic $Bi_3FeMo_2O_{12}$. $TlReO_4$ undergoes a rare re-entrant phase transition from its monoclinic polymorph to the tetragonal scheelite structure, concomitant with the loss of the ordering of the ReO_4 rotations, when heated above 400 °C.[28] In $Bi_3FeMo_2O_{12}$ the 2:1 ordering of the cations is stable at high temperatures and is retained upon cooling. A common feature between $TlReO_4$ and $Bi_3FeMo_2O_{12}$ is the presence of a cation with the $6s^2$ valence shell on the A site, Tl^+ and Bi^{3+}. We postulate that disruption of the oxygen lattice by the 6s lone pair electrons causes increased structural flexibility that facilitates ordering on the B site. The loss of ordering of the 6s lone pair electrons, either by heating in the case of $TlReO_4$ or through the use of a wet chemical synthetic approach for $Bi_3FeMo_2O_{12}$, allows the formation of the tetragonal phase. In other words, the distortion of the oxygen lattice due to the 6s lone pair of Bi^{3+} gives sufficient structural flexibility to facilitate the unusual ordering on the B-site.[7]

In this study, both the disordered tetragonal and ordered monoclinic forms of $Bi_3FeMo_2O_{12}$, have been synthesised and characterised using a variety of techniques. To examine the uncommon cation

ordering and nature of the tetragonal-to-monoclinic phase transition, we have characterized the crystal structure and magnetic properties of the compounds using a combination of X-ray powder diffraction (PXRD), high-resolution and variable-temperature (VT) neutron powder diffraction (NPD), transmission electron microscopy (TEM), scanning transmission electron microscopy (STEM), energy dispersive X-ray spectroscopy (EDS) and vibrating sample magnetometry (VSM).

Experimental methods

Sample preparation

The disordered tetragonal $Bi_3FeMo_2O_{12}$ phase was synthesised by a sol-gel method, following the general procedure described by Jeitschko *et al.*[7] Iron and bismuth nitrate powders (technical grade, Sigma-Aldrich) were dissolved in deionized water and 2 M HNO_3 respectively, to form 2 M $Fe(NO_3)_3 \cdot 9H_2O$ and 0.5 M $Bi(NO_3)_3 \cdot 5H_2O$ solutions. A 0.05 M aqueous solution of $(NH_4)_6Mo_7O_{24} \cdot 4H_2O$ (technical grade, Sigma-Aldrich) was prepared using deionized water. Appropriate amounts of each solution were mixed under constant magnetic stirring such that a Bi:Fe:Mo molar ratio of 3:1:2 was obtained, equal to that of the desired product. Ammonium hydroxide was then added dropwise under constant magnetic stirring until the pH of the mixture was ~7, giving rise to the formation of an orange precipitate. The mixture was then heated to a maximum temperature of ~280 °C until dry. The product was washed with water, to eliminate any possible residual NH_4NO_3, and dried in air at 80 °C.

To prepare the ordered monoclinic $Bi_3FeMo_2O_{12}$ phase, a portion of the synthesized disordered tetragonal phase was finely ground, pressed into a rod using a hydrostatic press, transferred to an alumina crucible, and annealed in a furnace at 550 °C for 24 h. This process (grinding, pressing into a rod and annealing) was repeated at 650 °C, 750 °C and 850 °C. The composition of the samples was confirmed using a combination of energy dispersive X-ray spectroscopy (EDS) and structural analysis. Neither the Rietveld analysis of the neutron diffraction data, nor the EDS results provided evidence for detectable amounts of oxygen vacancies in the samples.

Characterization

Powder X-ray diffraction data (PXRD) were collected using a PANalytical XPert Powder flat plate system equipped with a Cu anode and K_α radiation. High resolution neutron powder diffraction (NPD) data for both phases were measured using ECHIDNA at ANSTO's OPAL reactor at a wavelength of 1.622 or 2.44 Å.[36] Variable temperature (VT) NPD data were collected during heating of the disordered tetragonal $Bi_3FeMo_2O_{12}$ phase, from room temperature to 700 °C, using WOMBAT, the high-intensity powder

diffractometer at the OPAL reactor, ANSTO.[37] A temperature ramp of 2.5 °C/min was used, with a 5 min collection time.

Scanning transmission electron microscopy data were collected using a JEOL 2100F with a CEOS Cs aberration corrector using a 200 kV focused electron beam and a Fischione high angle annular darkfield detector (HAADF). The powders were lightly ground in an agate mortar and pestle before being loaded onto holey carbon-coated Cu TEM grids. A JEOL JEM2100F instrument with a CEOS aberration corrector for the electron probe was used at 200 kV to image the sample. The probe-forming aperture semi angle was 17.5 mrad, and the Fischione model 3000 ADF detector spanned 75−300 mrad. Images were acquired synchronously with ac electric power (60 Hz) to minimize 60 Hz artifacts in the images. A pixel dwell time of 15.7 μs was used throughout. The high-temperature *in situ* heating of the TEM specimen was done using a Fusion Select heating holder from Protochips allowing heating up to 1200 °C. The sample was deposited on a MEMS-based Fusion Select e-chip with a silicon carbide heating substrate with 8μm holes to which was applied a fabricated amorphous carbon thin film with 2μm holes. The specimen was heated in vacuum inside the microscope from room temperature to the target temperature at a rate of 10 °C/s followed by a hold at temperature for 5 minutes. The heating current was then turned off, quenching the specimen back to room temperature. Electron micrographs collected at room temperature following heat treatment to several temperatures, are given in the ESI.

Neutron total scattering data were collected at 100 K and 300 K using the Nanoscale Ordered MAterials Diffractometer (NOMAD)[38] at the Spallation Neutron Source (SNS) located at Oak Ridge National Laboratory (ORNL). The samples were loaded into 3 mm quartz capillaries. Software available at the beamline was used to calculate the Pair Distribution Function (PDF) from the NOMAD data. The PDF was calculated with a Q_{max} of 25 and 31.4 Å^{-1} for the disordered tetragonal and ordered monoclinic samples, respectively.

The macroscopic magnetic properties of the powder samples were measured using a DynaCool Quantum Design Physical Property Measurement System (PPMS) equipped with a vibrating sample magnetometer (VSM). For the magnetic measurements, the powders were inserted into measuring capsules and placed in a tubular brass sample holder. Zero-field-cooled (ZFC) and field-cooled (FC) curves were collected in the temperature range of 1.8 K – 300 K using an applied magnetic field of 1000 Oe. Field-dependent magnetization curves were collected at 1.8 K and 50 K, scanning the applied field in the range of ± 9 T.

Structural analysis

The powder diffraction data were analysed by Rietveld refinement using the FullProf Suite software package.[39] The peak profile was modelled using the Thompson-Cox-Hastings formulation of the pseudo-

Voigt function.[40] Finger's model was used,[41] to describe the peak asymmetry due to axial divergence in terms of finite sample and detector sizes. The instrumental contribution to the peak broadening was accounted for by performing Le Bail fits of a NIST LaB$_6$ 660b standard measured under the same conditions as the studied samples.[42, 43] From these LaB$_6$ fits, an instrumental resolution file was created and implemented in the refinements of the studied materials to de-convolute the instrumental and sample contributions to the peak width. For the Rietveld analysis, the zero shift, unit cell parameters, atomic positions and isotropic atomic displacement parameters were refined, as well as the Lorentzian refinable size (Y) and strain (X) parameters. When indicated, the atomic site occupation fraction of Bi was also refined. In the monoclinic structure the atomic displacement parameters of the oxygen atoms were constrained to be equal, due to the limited Q-rage accessible when using 2.44 Å neutrons. The bond valence sum (BVS) was calculated as $S_{ij} = \exp[(R_0 - R_{ij})/B]$, where R_{ij} is the observed bond length, R_0 is a tabulated constant for the (ideal) bond length (Bi^{3+} = 2.094, Fe^{3+} = 1.759, Mo^{6+} = 1.907), and B is an empirical constant taken to be 0.37.[44]

Results and Discussion

Structure and magnetism of the disordered tetragonal Bi$_3$FeMo$_2$O$_{12}$

A light orange crystalline powder of the disordered tetragonal scheelite polymorph of Bi$_3$FeMo$_2$O$_{12}$ was obtained by co-precipitation synthesis. To accurately determine the crystal structure and the atomic positions of both the heavy cations and light oxygen anions, a Rietveld refinement of neutron and X-ray powder diffraction data was performed. The structure was indexed to the tetragonal cell in space group $I4_1/a$ (#88) and refined with Fe occupying 1/3 of the Wyckoff 4a tetrahedral site, and Mo occupying the remaining 2/3, giving a random distribution of the Fe and Mo atoms within the structure. The observed peak broadening indicates that the synthesised crystallites are nanosized, with a refined isotropic size of 33(2) nm and a maximum strain of 46.57%.[39] The refined unit cell parameters at room temperature are $a = b = 5.3175(3)$ Å and $c = 11.6214(7)$ Å, in excellent agreement with the those reported by Jeitschko et al.[7] As evident from Figure 2 the sample is single phase and there are no apparent crystalline impurities. In order to obtain a satisfactory description of the relative peak intensities in the PXRD data, it was found necessary to refine the site occupancy of the Bi cation, with the refinements indicating that the Bi site was not fully occupied, see Table 1 and Table S3. There is a discrepancy in the refined occupation fraction of Bi from the refinement against the PXRD and NPD data, the latter being less reliable due to the similarity of the Fe, Mo and Bi neutron scattering lengths, these being 9.45, 6.71 and 8.53 fm respectively. This means that the weighted average scattering length of Fe and Mo is 7.62 fm, which is very similar to that of Bi. This reduces the applicability of neutron diffraction to detect small Bi deficiencies in the structures. For X-

rays, however, Bi scatters much more strongly than Fe and Mo, and therefore small changes in Bi content are strongly evident in PXRD data. The refinements against both data sets yielded atomic displacement parameters of Bi on the 4b site that are noticeably higher than that of the other elements, see Table 1 and Table S3. The diffraction patterns and Rietveld refinement of NPD and PXRD data are shown in Figure 2, and a representation of the crystal structure is given in Figure 1a.
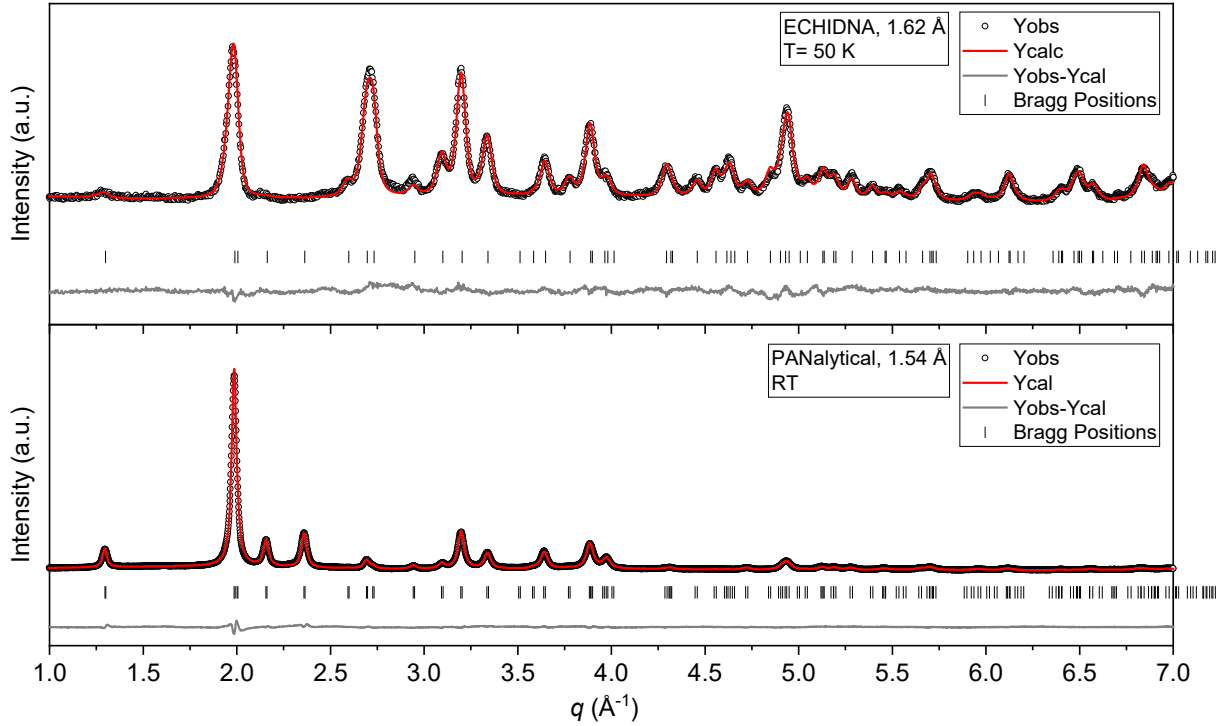

Figure 2: NPD (top) and PXRD (bottom) patterns and the resulting combined Rietveld refinement of both patterns in the tetragonal $I4_1/a$ $Bi_3FeMo_2O_{12}$ structure. The experimental data are shown as black circles, the refined model as a red line, the Bragg peak positions are indicated by the black vertical lines and difference between the experimental and refined intensity is shown in the lower grey line.

Table 1: Refined structural parameters for the disordered tetragonal structure at 50 K, from NPD data.

$Bi_3FeMo_2O_{12}$ – T=50 K – Disordered tetragonal, NPD						
Space group: $I4_1/a$ (No. 88), Z = 4/3						
Cell parameters: a=b= 5.3175(3) Å, c= 11.6214(7) Å, α=β=γ=90°, V=328.57(3) Å^3						
Crystallite size: 33(2) nm / maximum strain: 46.57%						
Fit quality: R_{Bragg}=5.58%, R_F=3.49%, χ^2_{global}=3.44						
Atom	Site	x	y	z	B_{iso} (Å^2)	SoF
Bi	4b	0.0	0.25	0.625	2.70(9)	0.91(1)
Fe	4a	0.0	0.25	0.125	0.93(5) ^{a}	0.333

8

| Mo | 4a | 0.0 | 0.25 | 0.125 | 0.93(5)[a] | 0.666 |
| O | 16f | 0.1567(3) | 0.0054(3) | 0.20899(16) | 1.41(4) | 1.000 |

[a] *Constrained to be equal for Fe and Mo, given that they are randomly distributed in the same site*

In the disordered tetragonal structure, the Fe and Mo cations occupy a 4a Wyckoff site, surrounded by four oxygen atoms in a tetrahedral coordination, as indicated in Figure 1a. The average (Fe/Mo)-O(1) distance is 1.8272(17) Å, with the BVS of Fe being 3.327(9) and of Mo 4.963(14), making the BVS of the combined site equal to 4.42(10). The Bi atoms are surrounded by eight oxygen atoms, and the average Bi-O(1) bond length is 2.4889(6) Å, with 4 shorter Bi-O bonds of 2.4758(17) Å and 4 longer bonds of 2.5019(18) Å, corresponding to a Bond Valence Sum (BVS) of 2.49. The diffraction data is consistent with the tetragonal space group $I4_1/a$. In this structure the eight Bi-O distances are approximately equal suggesting that there is no long-range ordering of the lone-pair electrons. Studies of scheelite-type oxides have shown that the Atomic Displacement Parameter (ADP) is typically larger for eight-coordinate A-type cation than for the four-coordinate B-type cation reflecting the greater freedom resulting from the longer A-O bond distances. It is possible that the larger ADP of the Bi cations, when compared with the remaining elements, observed here has a similar origin, noting that the magnitude of the refined ADP of the Bi cation is highly correlated with the occupancy of the Bi site An alternative explanation for the large Bi ADP is that there is some short-range disorder of the Bi cation, and this may also account for the variance in the Bi BVS. This is similar to the situation in some Bi containing pyrochlores, where the average structural analysis suggests the presence of displacive disorder of the Bi cations that is enhanced by the lone pairs. We developed and tested a model where the Bi was disordered from 4b to an equivalent 8e (0, 0.25, z) $z = 0.625$-x site, see the supplementary information, Table S3 and S4. This resulted in a comparable quality fit to the room temperature XRD and low temperature PND data with z~0.61, however it did not significantly change the magnitude of the refined ADP see ESI. Evidently, the lone pair electrons appear spatially averaged in the analysis of the Bragg diffraction data.

Magnetic properties

The temperature dependence of the zero-field cooled (ZFC) and field cooled (FC) magnetic susceptibilities for monoclinic $Bi_3FeMo_2O_{12}$ was reported recently,[45, 46] showing an antiferromagnetic transition with a T_N of approximately 11 K. However, no data has been reported on the magnetic properties of the tetragonal polymorph of $Bi_3FeMo_2O_{12}$. Our measurements for the tetragonal polymorph revealed no signs of long-range antiferromagnetic order down to 1.8 K,

although a slight divergence of the ZFC and FC susceptibilities emerges below 10 K (Figure 3a). Above 100 K the susceptibility displays Curie-Weiss type behaviour and the fit to this yielded a Curie-Weiss temperature, θ_{CW}, of -45.30(7) K and an effective magnetic moment per Fe^{3+} cation of 4.545(1) μ_B.

In accordance with previously reported data, the magnetization isotherms measured for the ordered monoclinic polymorph at 1.8 K and 50 K show linear behaviour, and do not saturate at fields of up to 9T confirming the absence of a ferromagnetic component (Figure S1 in ESI). The magnetization isotherms of the tetragonal disordered phase are more interesting. As shown in Figure 3b, at 50 K linear behaviour of the M-H curve is observed, consistent with the paramagnetic nature of the material deduced from the ZFC/FC curves. At 1.8 K, however, deviation from linearity is observed in the M-H curve, and a small opening of the hysteresis loop is observed, indicating some degree of ferro or ferrimagnetic behaviour.

The presence of ferromagnetism (FM) in the disordered tetragonal phase is unexpected, given both the lack of a magnetic transition in the ZFC/FC curves and the AFM order in the monoclinic structure. [45, 46] The negative deviation from the Curie-Weiss fit of the inverse susceptibility at low temperatures is consistent with FM order. A positive deviation from the Curie-Weiss fit was observed for the AFM monoclinic polymorph (Figure S2). The low temperature FM behaviour of the tetragonal structure is further discussed later.
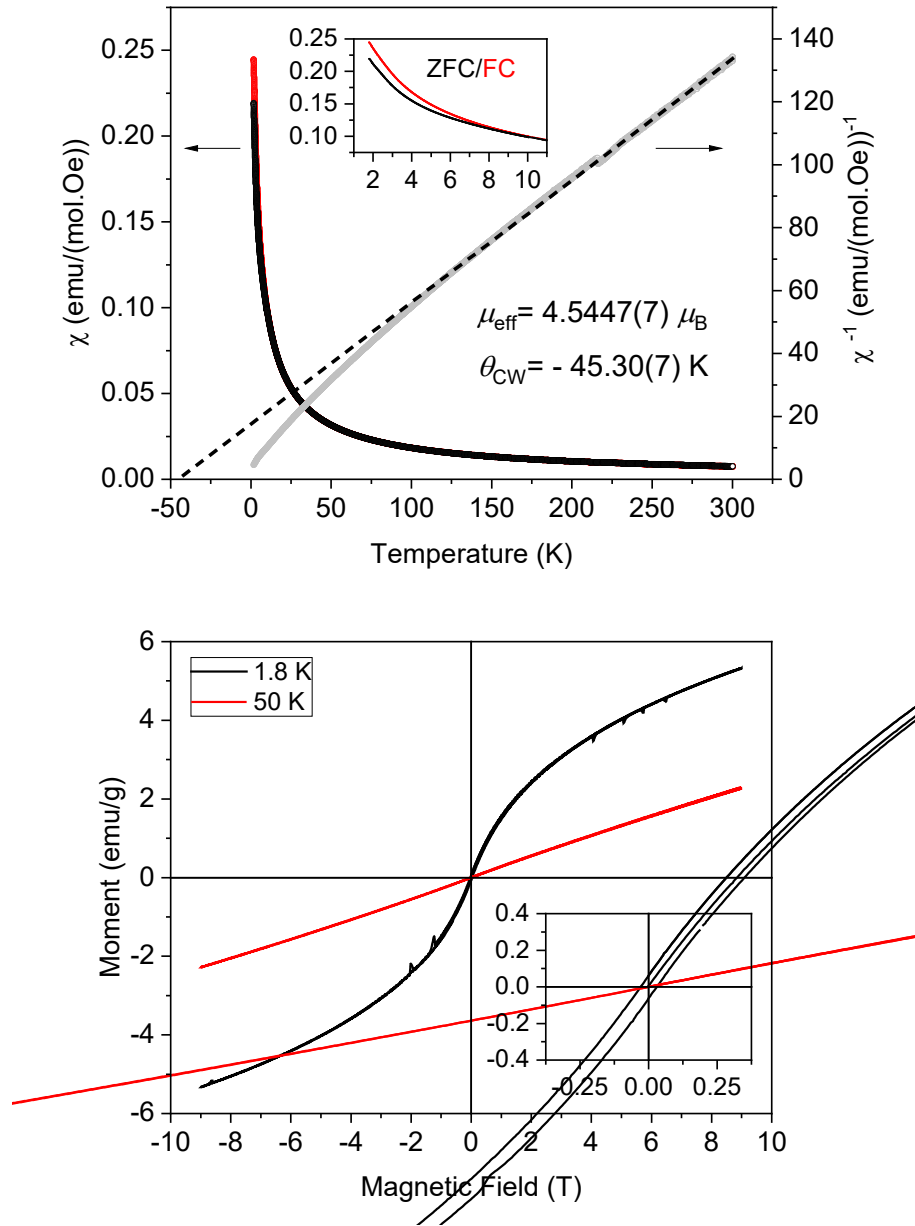
Figure 3: Upper Panel Magnetic susceptibility obtained from ZFC/FC curves and inverse magnetic susceptibility of the disordered tetragonal $Bi_3FeMo_2O_{12}$ phase collected from 1.8 K to 300 K at an applied field of 1000 Oe. The Curie-Weiss fit is shown as a black dashed line. Lower Panel Field-dependent magnetisation curves (+/- 9 T) of the disordered $Bi_3FeMo_2O_{12}$ structure measured at 1.8 K (black) and 50 K (red). The inset in (b) shows the opening of the magnetization curve at 1.8 K.

Structure of the ordered monoclinic $Bi_3FeMo_2O_{12}$

The as-synthesised tetragonal powders were annealed at a maximum temperature of 850 °C to obtain a green-yellow coloured sample of the monoclinic polymorph. Rietveld refinement of PXRD data

measured at room temperature verified the monoclinic $C2/c$ structure, see Figure 4, and showed the presence of a minor amount (1.0(1) wt.%) of Bi_2MoO_6 (see insert of Figure 4). The monoclinic $C2/c$ structure of $Bi_3FeMo_2O_{12}$ can be regarded as being built from three scheelite-like cells stacked along the a-axis with a 1:2 ordering of the Fe and Mo cations. This results in a tripling of the a-parameter as illustrated in Figure 1b. To ensure that ordering of Fe and Mo cations is actually taking place in the high-temperature structure, despite the relatively low transition temperature, Rietveld refinement of PXRD data were carried out with splitting of the Bi site but with random distribution of Fe and Mo cations in the tetrahedral site, akin to that of the $I4_1/a$ structure. It was readily observed that modelling a random distribution of Fe and Mo cations does not provide an adequate fit to the data, giving rise to clear discrepancies in the relative peak intensities, particularly pronounced at low Q (see Figure S3). This result confirms that both splitting of the Bi site and 2:1 ordering of the Mo and Fe cations along the a-axis is taking place in the annealed structure. A remarkable feature of the refinement is the full occupancy of the two crystallographically distinct bismuth sites. This suggests that a stoichiometric amount of bismuth must also be present in the as synthesised tetragonal sample. To confirm the composition of the samples energy dispersive X-ray spectroscopy (EDS) maps were collected for both the as synthesised and annealed powders (Figure S4). The elemental composition of both samples was, within the accuracy of the measurement, equal. This indicates that, despite the Bi deficiency evident from the Rietveld refinements of diffraction data collected on the tetragonal sample, no overall Bi deficiency is present. Given that no impurity phases were evident in the PXRD or NPD data of the as-synthesised tetragonal sample, the missing Bi is presumably present in a nano/amorphous state. This hypothesis is corroborated by HAADF STEM imaging following heating of the specimen as described below.

Neutron powder diffraction data was collected using the high-resolution diffractometer ECHIDNA[36] at 50 K and a wavelength of 2.44 Å, in order to extract precise atomic parameters and Bi-O distances. The results from the Rietveld refinement of the NPD data are presented in Table 2. Both the Fe and Mo cations have a distorted tetrahedral geometry, there being two distinct Fe-O distances of 1.881(7) Å and 1.896(6) Å resulting in a bond valence sum of 2.8 consistent with trivalent Fe. The geometry of the Mo cation is slightly more distorted with the Mo-O distances falling within a small range (1.749(7) – 1.814(7) Å), an average Mo-O distance of 1.783(4) Å and bond valence sum of 5.6.

The two crystallographically distinct Bi cations of the monoclinic polymorph are both in a distorted BiO_8 cube. Bi(1) occupies a $8f$ site and has three short bonds with Bi-O distances between 2.205(6) Å and 2.278(7) Å, and five longer bonds with Bi-O distances between 2.530(6) Å and 2.799(7) Å leading to an average Bi-O distance of 2.484(2) Å and bond valence sum of 3.2. Bi(2) occupies a $4e$ site with four short (2.199(6) - 2.318(6) Å) and four long (2.744(6) – 2.860(7) Å) Bi-O distances. The average Bi(2)-O distance is 2.529(2) Å and the bond valence sum is 3.2. The difference in the geometry of the two sites can

be understood as a consequence of different orientation of the Bi^{3+} $6s^2$ lone pair electrons.[7, 47] In the tetragonal scheelite structure the BiO_8 cube has two sets of approximately equidistant Bi-O contacts (four at 2.4758(17) Å and four at 2.5019(18) Å). In the Bi(1) site of the monoclinic structure the 6s lone pair is pointed towards a corner of the cube pushing a single oxygen, O(3), appreciably further away (2.799(7) Å), conversely in Bi(2) the lone pair points towards one of the faces of the original BiO_8 cube displacing the four O(5) oxygen atoms approximately equally (2.744(6) Å and 2.860(7) Å). Considering only the four short Bi-O contacts a $Bi(2)O_4$ square pyramid results. The coordination environment of both Bi cations and the corresponding Bi-O distances are illustrated in Figure 5.
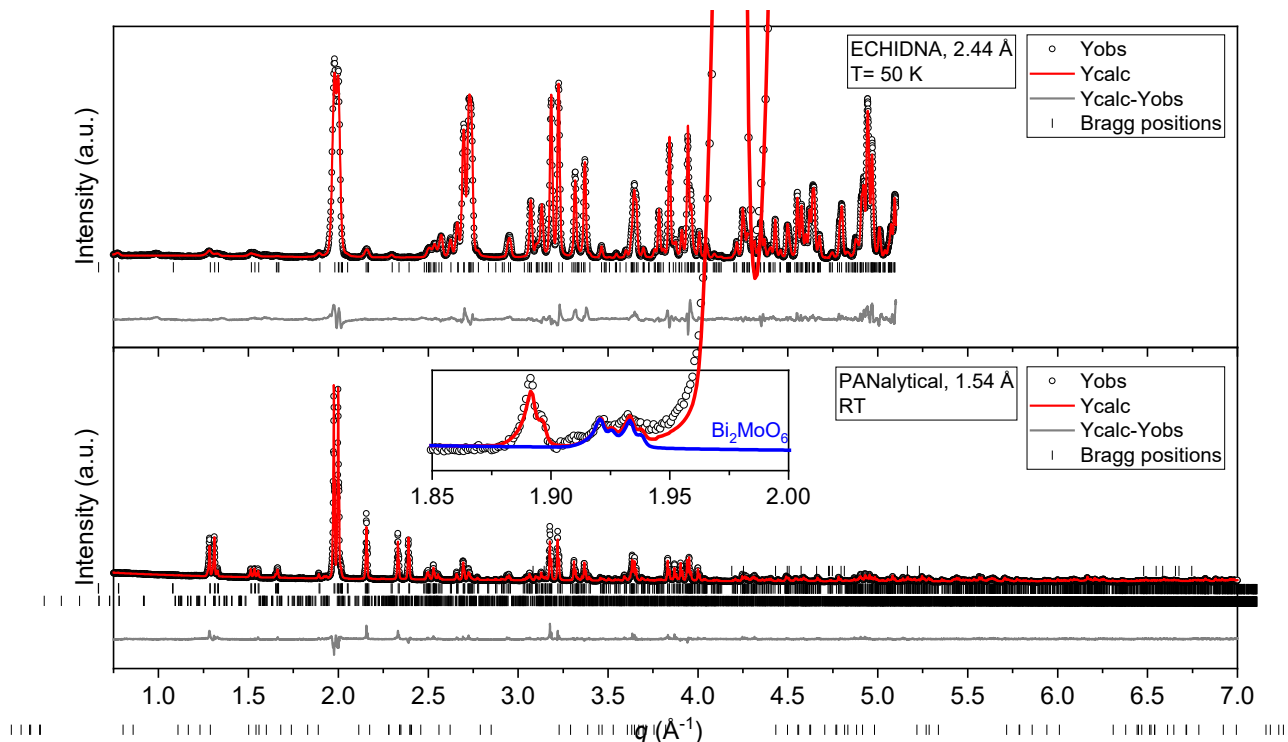

Figure 4: NPD (top) and PXRD (bottom) data and Rietveld refinement of monoclinic $Bi_3FeMo_2O_{12}$. The experimental data is represented by the black circles and the refined model by the red line. The positions of the space group allowed reflections are indicated by the black vertical lines and difference between experimental and refined intensities by the lower grey line. The insert of the PXRD illustrates the presence of 1.0(1) wt.% of Bi_2MoO_6 impurity (blue line). There are two minor peaks in the NPD data at $q \sim 1$ and 1.6 Å. The origin of these peaks could not be identified.

Table 2: Refined structural parameters for the ordered monoclinic structure at room temperature.

Bi$_3$FeMo$_2$O$_{12}$ – T= 50 K – Ordered monoclinic

Space group: $C2/c$ (No. 15), Z = 4

Cell parameters: a = 16.87959(18) Å, b = 11.61075(11) Å, c = 5.25017(5) Å, α= γ=90°, β=107.1931(6) °, V= 982.974(17) Å^3

Fit quality: R_{Bragg}=4.75%, R_F=3.08%, χ^2_{global}=16.0

Atom	Site	x	Y	z	B_{iso} (Å^2)	SoF
Bi(1)	8f	0.15175(16)	0.88716(27)	0.4074(7)	0.000(77)	1.00
Bi(2)	4e	0	0.6562(4)	0.25	0.21(12)	1.00
Fe	4e	0	0.1177(4)	0.25	0.00(10)	1.00
Mo	8f	0.16730(29)	0.3709(3)	0.4256(11)	0.00(9)	1.00
O(1)	8f	0.08648(31)	0.0422(5)	0.51098(94)	0.03(4)	1.00
O(2)	8f	0.04872(29)	0.2026(4)	0.030(1)	0.03(4)	1.00
O(3)	8f	0.21634(33)	0.2869(5)	0.2331(10)	0.03(4)	1.00
O(4)	8f	0.11462(34)	0.2910(4)	0.6193(11)	0.03(4)	1.00
O(5)	8f	0.09221(29)	0.4545(5)	0.2017(12)	0.03(4)	1.00
O(6)	8f	0.2471(3)	0.4599(4)	0.6450(12)	0.03(4)	1.00

The ADPs of the oxygen atoms were constrained to be equal. The smaller than typical ADPs are believed to be a result of the low temperature.
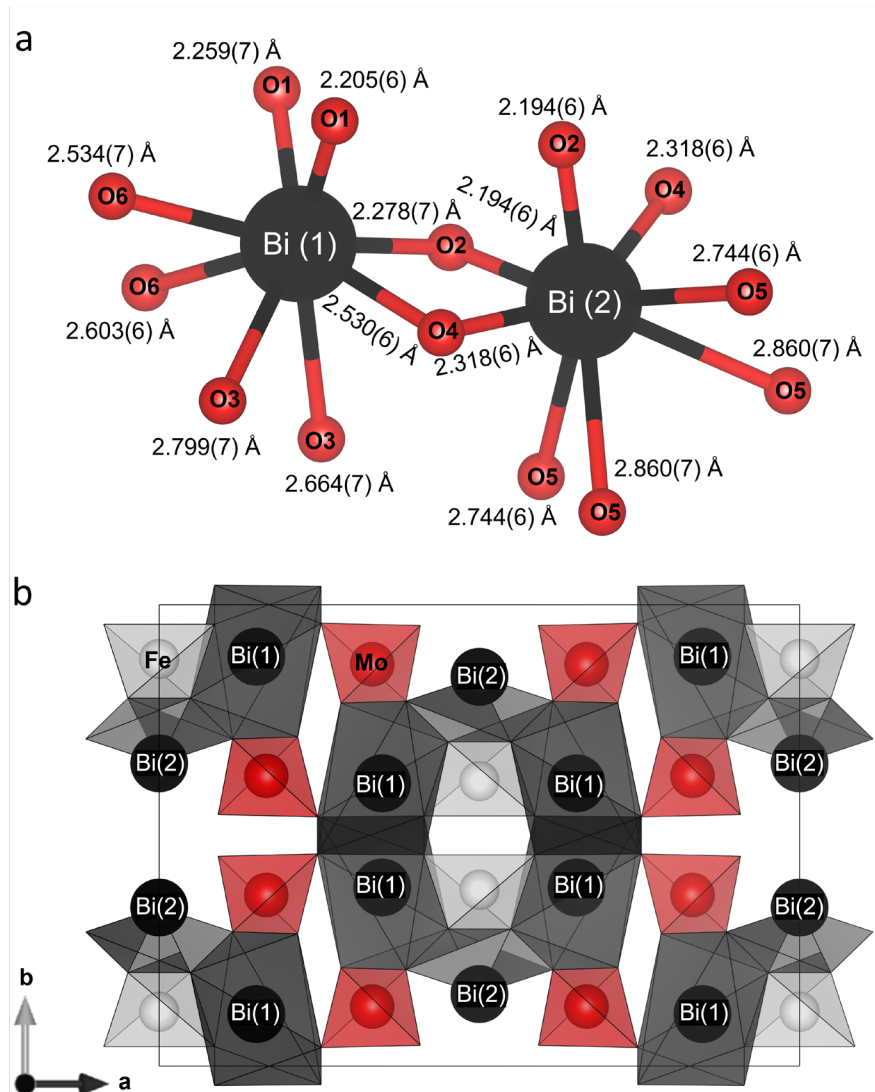
-

Figure 5: a) Representation of the Bi(1) and Bi(2) coordination to surrounding oxygen atoms in the monoclinic $C2/c$ structure of $Bi_3FeMo_2O_{12}$. The various Bi-O distances are shown. b) Monoclinic $Bi_3FeMo_2O_{12}$ showing black polyhedra formed by the Bi-O distances restricted to a maximum of 2.7 Å. Fe atoms are shown in grey and Mo atoms in red. Oxygen atoms are not shown but are located at the vertices of the polyhedra.

The impact of the lone pairs is highlighted in Figure 5b where only the Bi-O bonds that are 2.7 Å or shorter are considered. This reduces the Bi(2) to a square planar geometry whereas the Bi(1) reminds bonded to seven oxygen atoms. These are illustrated as black Bi-O polyhedral in Figure 5b, that clearly illustrate the difference between the Bi(1) and Bi(2) lone pair distortions. It is also apparent from this figure that the shorter Bi-O bonds are oriented towards the FeO_4 tetrahedra (depicted in grey) and the longer bonds towards the MoO_4 tetrahedra (depicted in red). Thus, there is an ordering of the lone pair electrons towards

15

the Mo cations. This can be compared to the presence of long B-O contacts in the related fergusonite structure of LnNbO$_4$ (Ln = lanthanoid) that expands the effective coordination of the B-type cation from 4 to 6.[27] This possibly reduces the underbonding of the Mo(VI) cation revealed in the BVS calculations.

Magnetic properties

Our measurement of the temperature dependence of the ZFC and FC magnetic susceptibilities for the monoclinic Bi$_3$FeMo$_2$O$_{12}$ sample agree with those previously reported (see Figure S2).[45, 46] The $C2/c$ polymorph of Bi$_3$FeMo$_2$O$_{12}$ behaves as a paramagnet until it orders antiferromagnetically on cooling below 12 K. The broad maximum observed around 12 K indicates the presence of short-range correlations.[45] There is evidence for a paramagnetic tail below 5 K. The inverse susceptibility follows the Curie-Weiss law above T_N. A Curie-Weiss fit over the temperature range $100 \leq$ T/K ≤ 300 yielded a Curie-Weiss temperature, θ_{CW}, of -25.50(7) K and an effective magnetic moment per Fe^{3+} cation of 5.834(1) μ_B.

HAADF STEM and EDS

High angle annular dark field scanning transmission electron microscopy (HAADF-STEM) images were collected on both, the tetragonal and monoclinic polymorphs. A different tetragonal sample to that described previously was used for the microscopy study. This sample had been heated for a shorter time in the last step of the co-precipitation synthesis and it therefore contained smaller crystallites of a much more nanosized nature, as demonstrated by the Rietveld analysis of PXRD data collected on the sample (see Figure S7 in ESI), which yielded crystallite sizes of 10.05(7) nm.

Representative HAADF-STEM images of the as-synthesised tetragonal polymorph are shown in Figure 6a-c. The sample is formed by agglomerates of very small nanoparticles between 3 to 6 nm in size, which is in good agreement with that obtained from the Rietveld analysis of PXRD data. When exposed to the 200 keV electron beam, the smaller particles exhibited local structural instabilities, with moving fringes as highlighted in Figure 6c. Movement of the small nanoparticles under the electron beam was observed. This possibly resembles the ordering process from tetragonal to monoclinic that takes place with annealing.

The as-synthesised tetragonal powder sample was annealed at 700 °C, and HAADF-STEM images were collected on the annealed product. Data show large particles of approximately 0.5 μm in size, with a highly ordered atomic structure (see Figure 6d-f). Figure 6f displays atomic resolution HR-STEM of the crystal structure along the (010) zone axis. Energy dispersive X-ray spectroscopy (EDS) maps of the as-synthesised and annealed powders, showing a homogeneous and stoichiometric elemental composition of the samples, are given in Figure S4.
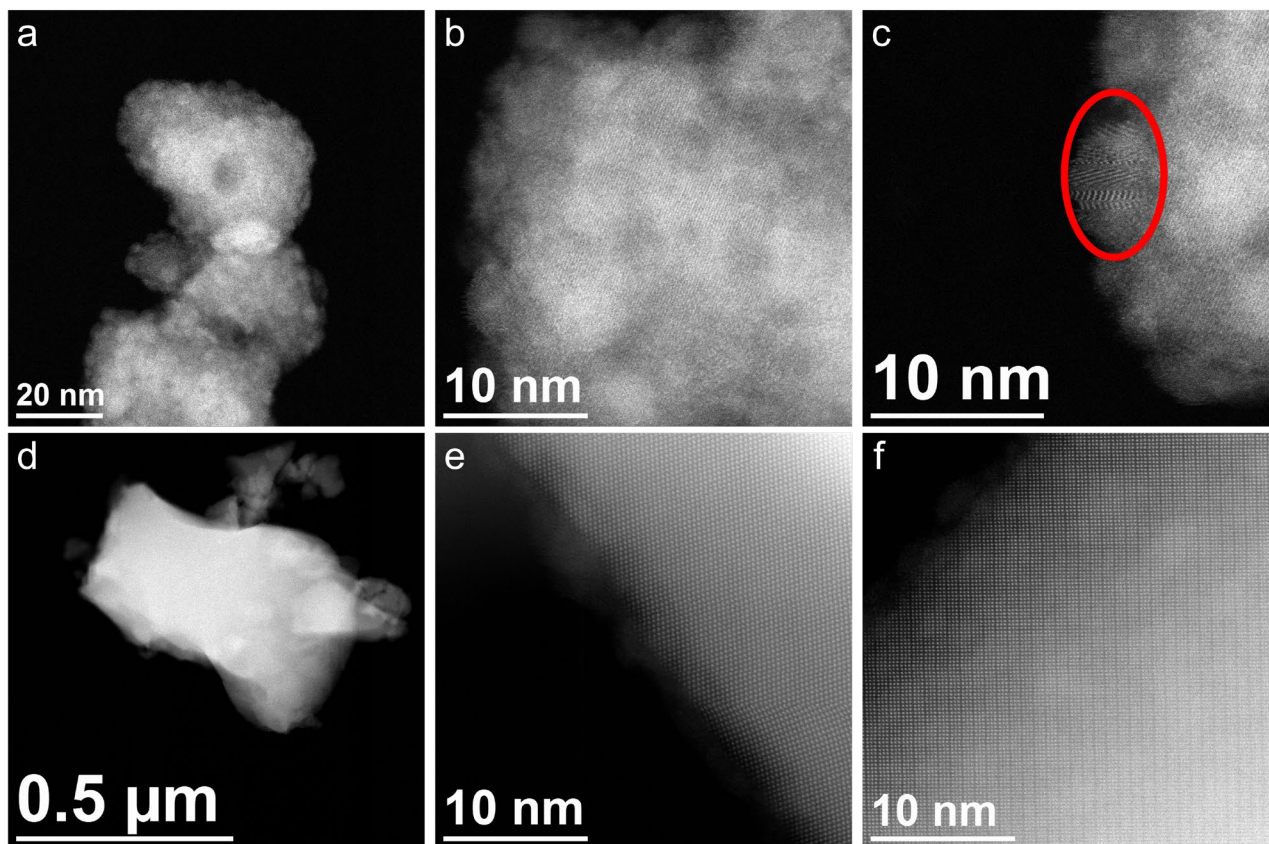
Figure 6: a-c: HR-STEM of as-synthesised tetragonal $Bi_3FeMo_2O_{12}$ showing agglomerates of small particles of 3-5 nm. Lattice planes are visible in b. The red circle in c shows local structural instabilities driven by the electron beam. d-f: HR-STEM of monoclinic $Bi_3FeMo_2O_{12}$ obtained by annealing the as-synthesised tetragonal sample, showing larger crystallites with a highly ordered atomic structure. The direction perpendicular to the image plane in f is the *b* axis.

Electron micrographs were collected at room temperature following heat treatment of the as-synthesised tetragonal $Bi_3FeMo_2O_{12}$ sample to several temperatures, and these are illustrated in Figure S8. HAADF STEM imaging reveals the formation of small 5-10 nm regions of the tetragonal phase at 300 ^{o}C. Furthermore, as shown in Figure S8 (350°C), small, disordered regions with a high Z-contrast appear which we attribute to disordered regions of bismuth that appear to phase separate during the initial stage of the phase transition to the monoclinic phase. This observation agrees with the analysis of the X-ray and neutron diffraction data that revealed a deficiency in the Bi site in the disordered tetragonal phase whereas the Bi sites in the ordered monoclinic phase are fully occupied. The fact that energy dispersive x-ray spectroscopy shows the same stoichiometry of the disordered tetragonal and the ordered monoclinic phase point to the presence of a minute amount of amorphous bismuth present in the latter. Since the contrast observed in

HAADF STEM imaging is independent of the degree of crystallinity, and largely depends on Z, we have an explanation for the small regions of higher contrast observed during the phase transition that is in agreement with the Rietveld analysis outlined above.

In situ NPD studies of the tetragonal-to-monoclinic phase transition

As noted above, the tetragonal $Bi_3FeMo_2O_{12}$ phase is metastable, and it can be converted to the ordered monoclinic phase by heating at relatively modest temperatures. There appears to be no information regarding the mechanism of the thermally induced conversion from disordered tetragonal to ordered monoclinic in $Bi_3FeMo_2O_{12}$. To investigate this transformation, *in situ* variable temperature (VT) neutron powder diffraction measurements from room temperature (RT) to 700 °C were undertaken. This *in situ* study was carried out using the same as-synthesised tetragonal sample that was used for the TEM analysis. As mentioned above, this sample consists of 10.05(7) nm crystallites, which are considerably smaller than those described in Figure 2 and Table 1, see also Figure S7.

Given the substantial cation movement required in the transformation from disordered tetragonal to order monoclinic structure, it was hypothesised that amorphization of the tetragonal polymorph and subsequent recrystallization into the ordered monoclinic would occur. This assumes that the highly charged Mo^{6+} and Fe^{3+} cations have very little mobility over the temperature range of interest. The formation of amorphous intermediates has been previously observed in phase transitions requiring significant atomic displacements.[48] However, as evident from Figure 7, no amorphization takes place, rather the tetragonal to monoclinic transformation takes place *via* a 1st order phase transition, with coexistence of both polymorphs evident over a temperature range of about 157 degrees (366-523 °C) as shown by the refined weight fractions as a function of temperature (Figure 8a).
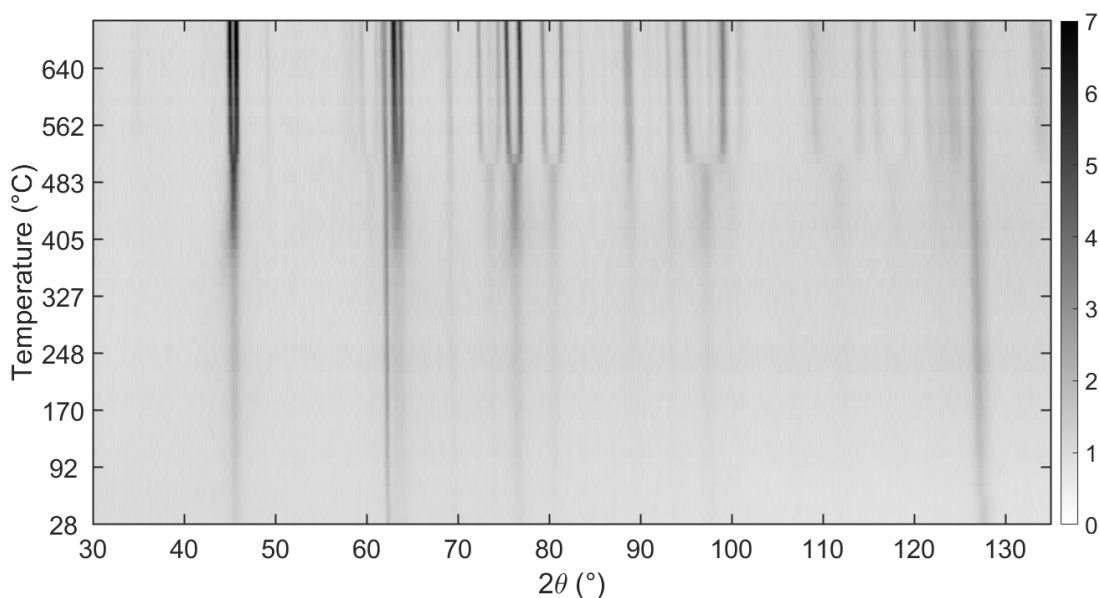
Figure 7: contour plot of the variable temperature NPD data illustrating the phase transition from tetragonal to monoclinic at approx. 500 °C. The NPD patterns are viewed from above, with color scale representing the diffracted intensity in a.u.

The results of Rietveld analysis of the VT-NPD data are summarised Figure 8. Examination of this figure suggests that the tetragonal-monoclinic transformation takes place through a three-stage process:

Stage 1.   Below about 366 °C the sample is single tetragonal phase. In the Rietveld refinements from these data the peak width was estimated using the Lorentzian refinable size parameter Y (see Fullprof manual for details).[39] As the temperature is increased from room temperature the peak width parameter shows a subtle increase, as indicated by the linear fit between RT and 366 °C shown in Figure 8b. The increase in this parameter would, in principle, indicate a reduction in the crystallite size. However, this is highly unlikely given that the sample was being heated. Instead, we believe that the increase in peak width indicates the emergence of increased microstrains, possibly due to small atomic displacements. The combination of the nanosized nature of the crystallites and the quality of the *in-situ* NPD data (see Figure 8d) does not allow for accurate quantification of these two effects (size vs. strain). Consequently, to avoid over-parametrization of the refinements, we choose to exclusively refine the size parameter.

Stage 2.   At a critical temperature of about 366 °C the first indication for the formation of the crystalline monoclinic phase is observed. In the HAADF STEM images this nucleation was observed near 300 °C. The amount of this phase increases gradually upon heating to 500 °C. Over this temperature range there is a rapid decrease in the peak width suggestive of an increase in

19

crystallite size and/or reduction of the microstrains in the tetragonal phase. That the peak width of the tetragonal phase continuously reduces as the monoclinic phase emerges suggests that these two processes are correlated, and that the formation of the monoclinic phase requires crystallites above a critical size.

Over the temperature range ~ 366 – 450 °C there is a small but noticeable reduction in the unit cell volume of the tetragonal phase. The observed contraction in the unit cell volume during the transformation from the tetragonal to monoclinic structures is believed to be a consequence of increased coherence in the arrangement of the Bi 6s lone pair electrons. A similar effect is observed in $TlReO_4$, and in the lead fluorapatite $Pb_5(VO_4)_3F$ where the unit cell volume of the lone pair ordered phases are noticeably smaller than those of the disordered phases.[5, 49] Extrapolation of the equivalent volume of the monoclinic phase (red dashed lines in Figure 8c) suggests a similar effect is observed here. The observed contraction in the cell in this stage 2 is anisotropic, as shown in Figure S9 of the ESI.

Stage 3.   By about 500 °C, approximately half of the sample has transformed to the ordered monoclinic phase, and the size of the remaining tetragonal crystallites has increased to 17.42(16) nm.   Above this temperature the remaining tetragonal material rapidly converts to monoclinic, such that above 520 °C the diffraction patterns can be fit using a single-phase monoclinic model.   As evident from Figure 8b increased heating to 700 °C results in a small reduction in the peak widths, reflecting this high crystallinity of the sample.   The unit cell volume shows approximately linear thermal expansion over this temperature range.

Selected NPD data and corresponding Rietveld refinements at each stage of the process are given in Figure 8d-f.
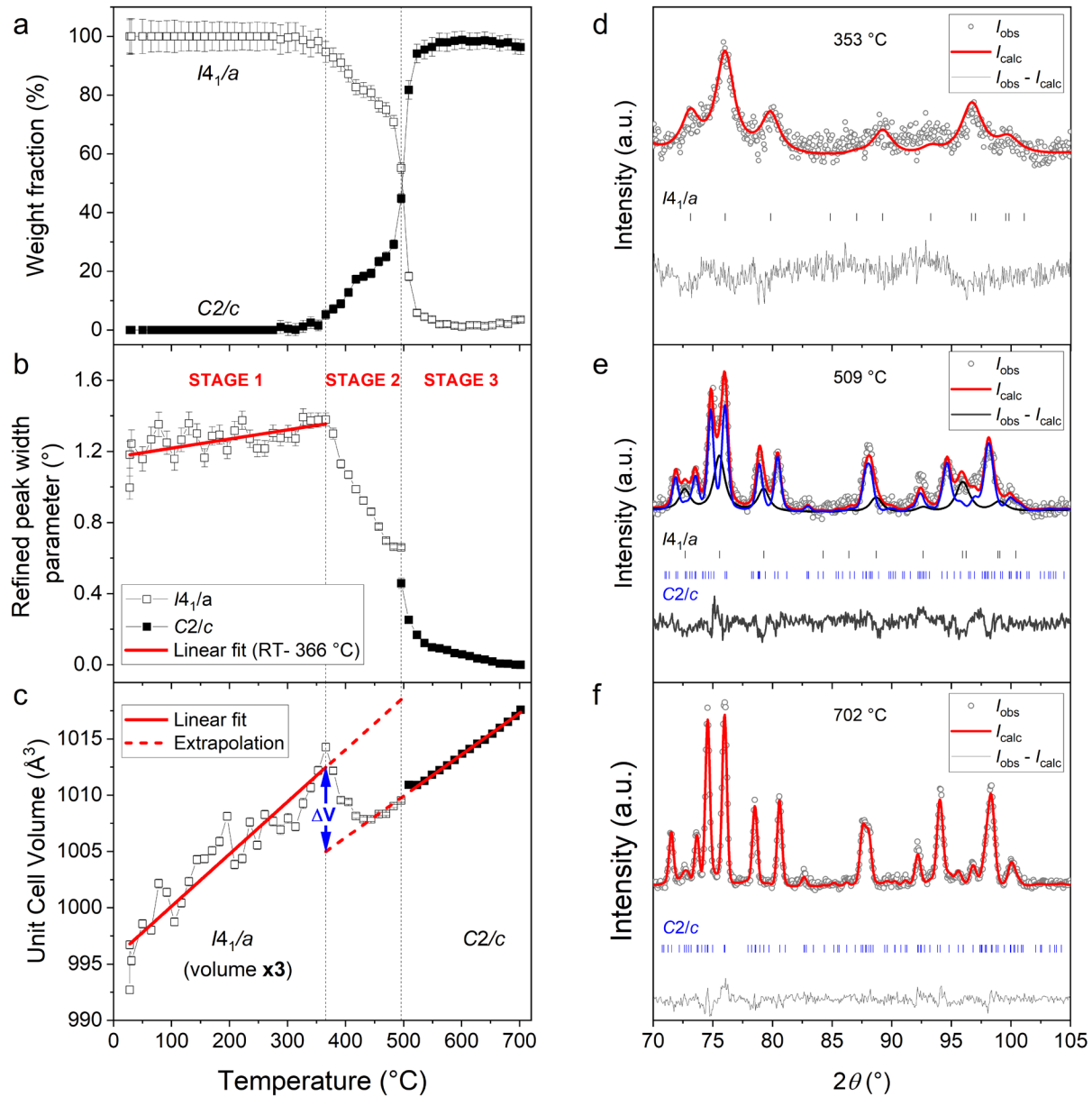
Figure 8: Refined values extracted from the *in situ* NPD studies of the transition from *I*4₁/*a* to *C*2/*c* in Bi₃FeMo₂O₁₂. a) Refined weight fractions as function of temperature. b) Refined peak width parameter, indicating the change in microstructure with temperature. c) Unit cell volume of the disordered tetragonal structure (*I*4₁/*a*) multiplied by 3, and of ordered monoclinic structure *C*2/*c*. The solid red lines are a linear fit of the unit cell volume of the two structures respectively, and the dashed lines extrapolate the linear fits to illustrate the reduction in unit cell volume (ΔV) of the *C*2/*c* structure compared to *I*4₁/*a*. d-f) Selected datasets and corresponding Rietveld refinements at three different temperatures: 353 C, 509 °C and 702 °C in d, e and f respectively. In e the relative contributions of the two phases are shown in black (*I*4₁/*a*) and blue (*C*2/*c*) together with the overall refinement profile in red. Where not apparent the error bars are smaller than the symbols.

Pair distribution function (PDF) analysis

Neutron total scattering data were measured for both the tetragonal and monoclinic polymorphs of $Bi_3FeMo_2O_{12}$ to establish the local structure in each. Structural refinements against the PDF data were conducted using the software TOPAS.[50] The Neutron-PDF (NPDF) data are shown in Figure 9 with fits using both the tetragonal and monoclinic structural models across $1.4 \leq r \leq 9.0$ Å presented for the un-annealed or LT phase. The fit across the full range is found in Figure S10. The first narrow peak in both NPDF, that occurs at ~ 1.8 Å, corresponds to the 1st Fe/Mo-O pair, *i.e.* that of the BO_4 tetrahedra. The first O-O distance, which corresponds to the edge of the tetrahedra, appears at ~ 2.90 Å. The remaining peaks between $2.0 \leq r \leq 3.5$ Å correspond to a mixture of the nearest neighbor Bi-O and subsequent O-O pairs.
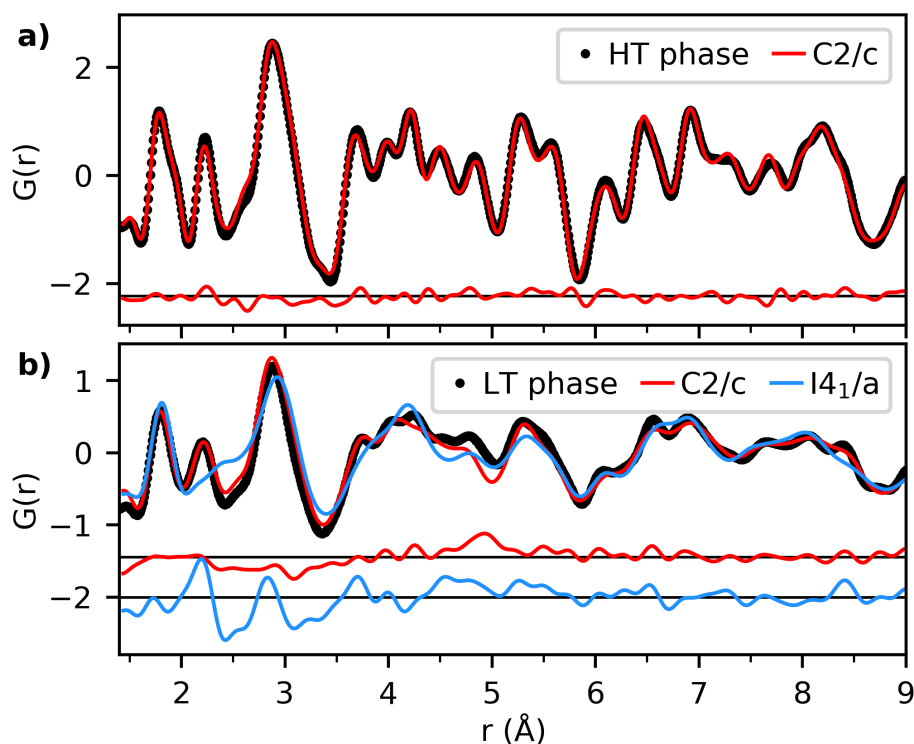

Figure 9: NPDF data at 100 K and refinement of a) high-temperature (HT) $Bi_3FeMo_2O_{12}$ (average monoclinic) and b) low temperature (LT) $Bi_3FeMo_2O_{12}$ (average tetragonal). The HT sample is fitted using the monoclinic C2/c structure and the LT sample is fitted using both, the C2/c (red) and the $I4_1/a$ (blue) structures. The black dots are the experimental data, the red and blue lines on top of the data are the calculated models, and the red/blue lines at the bottom of the plot are the difference between observed and calculated G(r).

For material annealed at high temperature the local and long-range structures are equivalent as shown by the excellent fit (Figure 9a) with the monoclinic model that has long-range ordering of the Bi^{3+} lone pairs. The excellent resolution of the NPDF data allows for the clear distinction between the Fe-O and Mo-O

distances at ~1.8 Å. Rietveld refinement against the neutron diffraction data showed that the Fe-O distance is slightly longer than the average Mo-O distance 1.894(8) vs 1.783(9) Å.

In the as-prepared sample the local structure is best described by the monoclinic model despite the long-range tetragonal symmetry evident from the X-ray diffraction data. This is shown by the superior NPDF fit with the monoclinic model, Figure 9b. This is most noticeable for $2.0 \leq r \leq 3.5$ Å, where the effect of the long and short Bi-O distances due to the lone-pair has a significant impact on the PDF. This demonstrates the presence of distorted BiO_8 polyhedra in the long-range tetragonal structure showing that the Bi^{3+} lone pairs are stereochemically active, but their orientation is not sufficiently correlated for the long-range monoclinic structure to form. The absence of resolved splitting in the first peak, at ~ 1.8 Å in the NPDF, that corresponds to the 1st Fe/Mo-O distances in the BO_4 tetrahedra is a consequence of the lower intensity data which results in a lower Q-max.

As noted above the lone-pair electrons are orientated towards the MoO_4 tetrahedra in the monoclinic polymorph and it is reasonable to postulate that a similar orientation will be present in the disordered tetragonal structure. This implies that locally the Fe and Mo cations are ordered in the tetragonal structure. That cation rearrangement is not required in the transformation from the tetragonal to monoclinic explains the absence of amorphization in the *in situ* diffraction measurements, and provides an explanation for the low temperature of this process. We note that the ordering of the Tl^+ lone pairs that drives the tetragonal to monoclinic transition in $TlReO_4$ is first order with both phases co-existing around the transition temperature. A similar occurrence is present in $Bi_3FeMo_2O_{12}$.

Whilst the NPDF studies show evidence for local ordering of the Bi 6s lone pair electrons, this alone should not result in the observed ferromagnetic behaviour displayed by the magnetization isotherms of the tetragonal $Bi_3FeMo_2O_{12}$ at 1.8 K, as evidenced by the anti-ferromagnetic (AFM) order in the monoclinic phase. The facile nature of the tetragonal to monoclinic transformation revealed by the *in situ* NPD studies suggest that the transformation is driven by a rearrangement of the oxygen sublattice. That is, local ordering of the iron and molybdenum cations is present in both phases but the limited coherence length of this leads to the appearance of the average tetragonal structure in the small crystallites. This is supported by the NPDF analysis. In their early studies of $Bi_3FeMo_2O_{12}$ Jietschko *et al.* concluded that their Mössbauer spectra provided evidence for a number of Fe^{3+} sites in the tetragonal phase, and we speculate that this may be a result of different orientation of the Bi 6s electrons.[7] Critically the Mössbauer parameters for the major phase in the tetragonal phase were the same as those of the ordered monoclinic phase. The loss of ferromagnetism that accompanies the tetragonal to monoclinic transformation does not appear to be a consequence of the change in the iron-molybdenum cation ordering nor in the short-range ordering of the Bi 6s lone pairs. There are two plausible explanations for the FM; either it reflects the presence of superparamagnetism or that this is a result of the presence of defects, and in particular oxygen vacancies,

in the nanosized crystallites of the tetragonal phase.[51, 52] Nanomaterials, with their high surface to volume ratio, typically contain large numbers of surface defects and there is growing consensus that surface defects such as oxygen vacancies can lead to weak ferromagnetism, although the precise mechanism for this remains unclear.[53] Oxygen vacancies will also induce lattice defects that can alter the nature of the super exchange interactions potentially favouring ferrimagnetic exchange.

Conclusions

The unusual symmetry lowering in the complex scheelite oxide $Bi_3FeMo_2O_{12}$ at high temperatures has been studied using a variety of methods. Rietveld Refinement of X-ray and neutron powder diffraction data show that the average structure of $Bi_3FeMo_2O_{12}$, prepared using a low temperature sol-gel approach, is tetragonal where the Fe and Mo are disordered at the center of oxygen tetrahedra. This tetragonal model requires that there is no coherent, long-range ordering of the Bi $6s^2$ lone pair electrons; that is they do not appear to be stereochemically active. Heating the sample above 500 °C results in a first order structural transformation to a monoclinic structure in which the Fe and Mo cations order over different sites. This monoclinic structure also has two fully occupied crystallographically distinct Bi sites, in which the Bi 6s electrons exhort a stereochemical influence with different orientations. The transition between the two structures results in a reduction in the unit cell volume, analogous to that seen in $TlReO_4$ [5] and $Pb_5(VO_4)_3F$,[49] where the unit cell volume of the lone pair ordered phases are noticeably smaller than that of the disordered phases. This is a consequence of the well-known distortion theorem. [54]

Neutron Pair Distribution Function (NPDF) analysis shows that, for the material annealed at high temperature, the local and long-range structures are equivalent with the monoclinic model revealing long-range ordering of the Bi^{3+} lone pairs. The NPDF of the as-synthesised material cannot be explained using the disordered tetragonal model, rather this shows evidence for distortion of the BiO_8 polyhedra indicative of local ordering of the Bi^{3+} lone pairs. Thus, $Bi_3FeMo_2O_{12}$ is an unusual example of a complex oxide that undergoes a symmetry lowering transition upon heating as a consequence of long-range ordering of the 6s lone pair electrons.

Bulk magnetic susceptibility measurements of the as-synthesised tetragonal material showed a slight divergence of the ZFC and FC susceptibilities below 10 K and an opening of the low temperature magnetization isotherm showing the presence of weak ferromagnetic ordering. This contrasts to the antiferromagnetic ordering evident in the annealed monoclinic material. It is believed that the observed ferromagnetism is a consequence of defects in the nanosized crystallites of the tetragonal phase.

Conflicts of interest

There are no conflicts of interest to declare.

Supporting Information

The Supporting Information is available free of charge at https://pubs.acs.org
Details on refined structural parameters for the disordered tetragonal polymorph of $Bi_3FeMo_2O_{12}$ at room temperature. Magnetic characterization (ZFC/FC curves and magnetization curves) of monoclinic $Bi_3FeMo_2O_{12}$. (S)TEM-EDS maps of as-synthesized (average tetragonal) and annealed (monoclinic) samples. PXRD data and Rietveld refinement of low temperature (average tetragonal) $Bi_3FeMo_2O_{12}$ powder sample heated for shorter time in the synthesis process, illustrating the broad diffraction peaks characteristic of nanosized crystallites. Example of fits to alternate models. Refined lattice parameters of as-synthesized $Bi_3FeMo_2O_{12}$ upon heating from room temperature to 500 °C. (PDF)

Acknowledgements

References

1.   Walsh, A.; Payne, D. J.; Egdell, R. G.; Watson, G. W., Stereochemistry of post-transition metal oxides: revision of the classical lone pair model. *Chemical Society Reviews* **2011,** *40* (9), 4455-4463.

2.   Walsh, A.; Watson, G. W., The origin of the stereochemically active Pb(II) lone pair: DFT calculations on PbO and PbS. *Journal of Solid State Chemistry* **2005,** *178* (5), 1422-1428.

3.   Zhang, N.; Yokota, H.; Glazer, A. M.; Thomas, P. A., The not so simple cubic structure of $PbZr_{1-x}Ti_xO_3$ (PZT): complex local structural effects in perovskites. *Acta Crystallographica Section B* **2011,** *67* (6), 461-466.

4.   Knox, K. R.; Bozin, E. S.; Malliakas, C. D.; Kanatzidis, M. G.; Billinge, S. J. L., Local off-centering symmetry breaking in the high-temperature regime of SnTe. *Physical Review B* **2014,** *89* (1), 014102.

5.   Saura-Múzquiz, M.; Marlton, F. P.; Mullens, B. G.; Manjón-Sanz, A. M.; Neuefeind, J. C.; Everett, M.; Brand, H. E. A.; Mondal, S.; Vaitheeswaran, G.; Kennedy, B. J., Understanding the Re-entrant Phase Transition in a Non-magnetic Scheelite. *Journal of the American Chemical Society* **2022,** *144* (34), 15612-15621.

6.   Fabini, D. H.; Laurita, G.; Bechtel, J. S.; Stoumpos, C. C.; Evans, H. A.; Kontos, A. G.; Raptis, Y. S.; Falaras, P.; Van der Ven, A.; Kanatzidis, M. G.; Seshadri, R., Dynamic Stereochemical Activity of the Sn^{2+} Lone Pair in Perovskite $CsSnBr_3$. *Journal of the American Chemical Society* **2016,** *138* (36), 11820-11832.

7.   Jeitschko, W.; Sleight, A. W.; Mcclellan, W. R.; Weiher, J. F., A Comprehensive Study of Disordered and Ordered Scheelite-Related $Bi_3(FeO_4)(MoO_4)_2$. *Acta Crystallogr B* **1976,** *32* (Apr15), 1163-1170.

8.   Getsoian, A. B.; Zhai, Z.; Bell, A. T., Band-Gap Energy as a Descriptor of Catalytic Activity for Propene Oxidation over Mixed Metal Oxide Catalysts. *Journal of the American Chemical Society* **2014,** *136* (39), 13684-13697.

9.   Van Den Elzen, A. F.; Rieck, G. D., The crystal structure of $Bi_2(MoO_4)_3$. *Acta Crystallographica Section B* **1973,** *29* (11), 2433-2436.

10.   Chen, H.-Y.; Sleight, A. W., Crystal structure of $Bi_2Mo_2O_9$: A selective oxidation catalyst. *Journal of Solid State Chemistry* **1986,** *63* (1), 70-75.

11.   Teller, R. G.; Brazdil, J. F.; Grasselli, R. K.; Jorgensen, J. D., The structure of γ-bismuth molybdate, Bi_2MoO_6, by powder neutron diffraction. *Acta Crystallographica Section C* **1984,** *40* (12), 2001-2005.

12.   Brazdil, J. F., Scheelite: a versatile structural template for selective alkene oxidation catalysts. *Catalysis Science & Technology* **2015,** *5* (7), 3452-3458.

13.   Bastide, J. P., Simplified systematics of the compounds ABX_4 ($X=O^{2-},F^-$) and possible evolution of their crystal-structures under pressure. *Journal of Solid State Chemistry* **1987,** *71* (1), 115-120.

14.   Wang, Z.; Liang, H.; Gong, M.; Su, Q., Luminescence investigation of Eu^{3+} activated double molybdates red phosphors with scheelite structure. *Journal of Alloys and Compounds* **2007,** *432* (1), 308-312.

15.   Xiao, B.; Schmidt, M., Incorporation of Europium(III) into Scheelite-Related Host Matrixes ABO_4 (A = Ca^{2+}, Sr^{2+}, Ba^{2+}; B = W^{6+}, Mo^{6+}): Role of A and B Sites on the Dopant Site Distribution and Photoluminescence. *Inorganic Chemistry* **2017,** *56* (24), 14948-14959.

16.   Shen, X.; Zhou, L.; Chai, Y.; Wu, Y.; Liu, Z.; Yin, Y.; Cao, H.; Cruz, C. D.; Sun, Y.; Jin, C.; Muñoz, A.; Alonso, J. A.; Long, Y., Large linear magnetoelectric effect and field-induced ferromagnetism and ferroelectricity in $DyCrO_4$. *NPG Asia Materials* **2019,** *11* (1), 50.

17.   Yang, X.; Fernández-Carrión, A. J.; Wang, J.; Porcher, F.; Fayon, F.; Allix, M.; Kuang, X., Cooperative mechanisms of oxygen vacancy stabilization and migration in the isolated tetrahedral anion Scheelite structure. *Nature Communications* **2018,** *9* (1), 4484.

18.   Esaka, T., Ionic conduction in substituted scheelite-type oxides. *Solid State Ionics* **2000,** *136-137*, 1-9.

19.   Lv, J.; Dai, K.; Zhang, J.; Geng, L.; Liang, C.; Liu, Q.; Zhu, G.; Chen, C., Facile synthesis of Z-scheme graphitic-C_3N_4/Bi_2MoO_6 nanocomposite for enhanced visible photocatalytic properties. *Applied Surface Science* **2015,** *358*, 377-384.

20.   Feng, Y.; Yan, X.; Liu, C.; Hong, Y.; Zhu, L.; Zhou, M.; Shi, W., Hydrothermal synthesis of CdS/Bi_2MoO_6 heterojunction photocatalysts with excellent visible-light-driven photocatalytic performance. *Applied Surface Science* **2015,** *353*, 87-94.

21.   Tokunaga, S.; Kato, H.; Kudo, A., Selective Preparation of Monoclinic and Tetragonal $BiVO_4$ with Scheelite Structure and Their Photocatalytic Properties. *Chemistry of Materials* **2001,** *13* (12), 4624-4628.

22.   Liu, T.; Zhang, X.; Guan, J.; Catlow, C. R. A.; Walsh, A.; Sokol, A. A.; Buckeridge, J., Insight into the Fergusonite–Scheelite Phase Transition of ABO_4-Type Oxides by Density Functional Theory: A Case Study of the Subtleties of the Ground State of $BiVO_4$. *Chemistry of Materials* **2022,** *34* (12), 5334-5343.

23.   Clavier, N.; Podor, R.; Dacheux, N., Crystal chemistry of the monazite structure. *Journal of the European Ceramic Society* **2011,** *31* (6), 941-976.

24.   Rögner, P.; Range, K.-J., The crystal structure of β-Thallium perrhenate. *Zeitschrift für anorganische und allgemeine Chemie* **1993,** *619* (6), 1017-1022.

25.   Rögner, P.; Range, K.-J., Notizen: The Crystal Structure of β-$CsReO_4$, the Room-Temperature Modification of Cesium Perrhenate. *Zeitschrift für Naturforschung B* **1993,** *48* (5), 685.

26.   Rögner, P.; Range, K.-J., Strukturverfeinerung von Rubidiumperrhenat bei 297 und 159 K. *Zeitschrift für Naturforschung B* **1993,** *48* (2), 233.

27.   Arulnesan, S. W.; Kayser, P.; Kimpton, J. A.; Kennedy, B. J., Studies of the fergusonite to scheelite phase transition in $LnNbO_4$ orthoniobates. *Journal of Solid State Chemistry* **2019,** *277*, 229-239.

28.   Chay, C.; Avdeev, M.; Brand, H. E. A.; Injac, S.; Whittle, T. A.; Kennedy, B. J., Crystal structures and phase transition behaviour in the 5d transition metal oxides $AReO4$ (A = Ag, Na, K, Rb, Cs and Tl). *Dalton Trans* **2019,** *48* (47), 17524-17532.

29.   Injac, S.; Yuen, A. K. L.; Avdeev, M.; Wang, C. H.; Turner, P.; Brand, H. E. A.; Kennedy, B. J., Structural and Magnetic Studies of ABO_4-Type Ruthenium and Osmium Oxides. *Inorganic Chemistry* **2020,** *59* (5), 2791-2802.

30.   Kennedy, B. J.; Injac, S.; Thorogood, G. J.; Brand, H. E. A.; Poineau, F., Structures and Phase Transitions in Pertechnetates. *Inorganic Chemistry* **2019,** *58* (15), 10119-10128.

31.   Sleight, A. W.; Aykan, K.; Rogers, D. B., New nonstoichiometric molybdate, tungstate, and vanadate catalysts with the scheelite-type structure. *Journal of Solid State Chemistry* **1975,** *13* (3), 231-236.

32.   Sleight, A. W.; Jeitschko, W., $Bi_3(FeO_4)(MoO_4)_2$ and $Bi_3(GaO_4)(MoO_4)_2$ - New Compounds with Scheelite Related Structures. *Mater Res Bull* **1974,** *9* (7), 951-954.

33.   Klevtsov, P. V.; Klevtsova, R. F., Polymorphism of the double molybdates and tungstates of mono- and trivalent metals with the composition $M^+R^{3+}(EO_4)_2$. *Journal of Structural Chemistry* **1977,** *18* (3), 339-355.

34.   Kolesov, B. A.; Kozeeva, L. P., Raman study of cation distribution in the scheelite-like double molybdates and tungstates. *Journal of Structural Chemistry* **1994,** *34* (4), 534-539.

35.   Lacorre, P.; Pautonnier, A.; Coste, S.; Barré, M.; Béchade, E.; Suard, E., Cationic Order–Disorder in Double Scheelite Type Oxides: the Case Study of Fergusonite La_2SiMoO_8. *Inorganic Chemistry* **2021,** *60* (4), 2623-2638.

36.   Avdeev, M.; Hester, J. R., ECHIDNA: a decade of high-resolution neutron powder diffraction at OPAL. *Journal of Applied Crystallography* **2018,** *51* (6), 1597-1604.

37.   Studer, A. J.; Hagen, M. E.; Noakes, T. J., Wombat: The high-intensity powder diffractometer at the OPAL reactor. *Physica B: Condensed Matter* **2006,** *385-386*, 1013-1015.

38.   Neuefeind, J.; Feygenson, M.; Carruth, J.; Hoffmann, R.; Chipley, K. K., The Nanoscale Ordered MAterials Diffractometer NOMAD at the Spallation Neutron Source SNS. *Nuclear Instruments and Methods in Physics Research Section B: Beam Interactions with Materials and Atoms* **2012,** *287*, 68-75.

39.   Rodriguez-Carvajal, J., Recent Advances in Magnetic-Structure Determination by Neutron Powder Diffraction. *Physica B: Condensed Matter* **1993,** *192* (1-2), 55-69.

40.   Thompson, P.; Cox, D. E.; Hastings, J. B., Rietveld Refinement of Debye-Scherrer Synchrotron X-Ray Data from Al_2O_3. *Journal of Applied Crystallography* **1987,** *20*, 79-83.

41.   Finger, L. W.; Cox, D. E.; Jephcoat, A. P., A correction for powder diffraction peak asymmetry due to axial divergence. *Journal of Applied Crystallography* **1994,** *27* (6), 892-900.

42.   Le Bail, A.; Duroy, H.; Fourquet, J. L., Ab-initio structure determination of $LiSbWO_6$ by X-ray powder diffraction. *Mater Res Bull* **1988,** *23* (3), 447-452.

43.   NIST SRM 660c; LaB_6; National Institute of Standards and Technology; U.S. Department of Commerce: Gaithersburg, MD (29 October 2015). https://www-s.nist.gov/srmors/certificates/660b.pdf.

44.   Brese, N.; O'keeffe, M., Bond-valence parameters for solids. *Acta Crystallographica Section B: Structural Science* **1991,** *47* (2), 192-197.

45.   Boya, K.; Nam, K.; Manna, A. K.; Kang, J.; Lyi, C.; Jain, A.; Yusuf, S. M.; Khuntia, P.; Sana, B.; Kumar, V.; Mahajan, A. V.; Patil, D. R.; Kim, K. H.; Panda, S. K.; Koteswararao, B., Magnetic properties of the S = 5/2 anisotropic triangular chain compound $Bi_3FeMo_2O_{12}$. *Physical Review B* **2021,** *104* (18), 184402.

46.   Li, C.; Gao, Z.; Tian, X.; Zhang, J.; Ju, D.; Wu, Q.; Lu, W.; Sun, Y.; Cui, D.; Tao, X., Bulk crystal growth and characterization of the bismuth ferrite-based material $Bi_3FeO_4(MoO_4)_2$. *CrystEngComm* **2019,** *21* (15), 2508-2516.

47.   Brown, I. D., Bond valence as an aid to understanding the stereochemistry of O and F complexes of Sn(II), Sb(III), Te(IV), I(V) and Xe(VI). *Journal of Solid State Chemistry* **1974,** *11* (3), 214-233.

48.   Pandelus, S. B.; Kennedy, B. J.; Murphy, G.; Brand, H. E.; Keegan, E.; Pring, A.; Popelka-Filcoff, R. S., Phase Analysis of Australian Uranium Ore Concentrates Determined by Variable Temperature Synchrotron Powder X-ray Diffraction. *Inorganic Chemistry* **2021,** *60* (15), 11569-11578.

49.   Oka, K.; Takasu, M.; Nishiki, W.; Nishikubo, T.; Azuma, M.; Noma, N.; Iwasaki, M., Negative Thermal Expansion in Fluoroapatite $Pb_5(VO_4)_3F$ Enhanced by the Steric Effect of Pb^{2+}. *Inorganic Chemistry* **2022,** *61* (32), 12552-12558.

50.   Coelho, A., TOPAS and TOPAS-Academic: an optimization program integrating computer algebra and crystallographic objects written in C++. *Journal of Applied Crystallography* **2018,** *51* (1), 210-218.

51.   Jaiswar, S.; Mandal, K. D., Evidence of Enhanced Oxygen Vacancy Defects Inducing Ferromagnetism in Multiferroic $CaMn_7O_{12}$ Manganite with Sintering Time. *The Journal of Physical Chemistry C* **2017,** *121* (36), 19586-19601.

52.   Sundaresan, A.; Bhargavi, R.; Rangarajan, N.; Siddesh, U.; Rao, C. N. R., Ferromagnetism as a universal feature of nanoparticles of the otherwise nonmagnetic oxides. *Physical Review B* **2006,** *74* (16), 161306.

53.   Choi, H.; Song, J. D.; Lee, K.-R.; Kim, S., Correlated Visible-Light Absorption and Intrinsic Magnetism of $SrTiO_3$ Due to Oxygen Deficiency: Bulk or Surface Effect? *Inorganic Chemistry* **2015,** *54* (8), 3759-3765.

54.   Woodward, P. M.; Karen, P.; Evans, J. S. O.; Vogt, T., *Solid State Materials Chemistry*. Cambridge University Press: Cambridge, 2021.

For Table of Contents Only
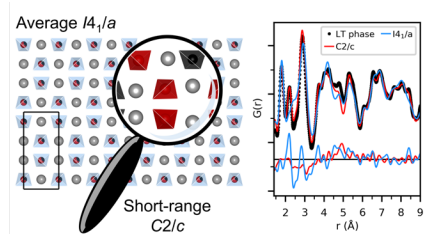
The role of the stereochemical activity and correlation length of Bi^{3+} $6s^2$ lone pairs is examined in relation to the rare symmetry lowering and 2:1 cation ordering of $Bi_3FeMo_2O_{12}$ upon heating.